Torque Modeling of a Segmented-Rotor SRM Using Maximum-Correntropy-Criterion-Based LSSVR for Torque Calculation of EVs

Xiaodong Sun, *Senior Member, IEEE*, Jiangling Wu, Gang Lei, *Member, IEEE*, Yingfeng Cai, *Member, IEEE*, Xiaobo Chen, and Youguang Guo, *Senior Member, IEEE*

***Abstract*—The high nonlinearities of switched reluctance motor (SRM) caused by its double salient structure limit its industrial application in electric vehicles (EVs). In this paper, an algorithm called maximum-correntropy-criterion-based least squares support vector regression (MCC-LSSVR) is applied to the nonlinear modeling of a segmented-rotor switched reluctance motor (SSRM). First, the mathematic model of the SSRM is established. Finite element analysis (FEA) is carried out to obtain the static flux linkage and torque. Then, the intelligent algorithm MCC-LSSVR using an adaptive weight to avoid the interference of outliers is introduced. It is verified and applied to SSRM modeling. The results show that the MCC-LSSVR exhibits a better performance than other intelligent algorithms. Finally, simulation and experimental validation under various modes are given to verify the accuracy and effectiveness of the MCC-LSSVR model. It is shown that the simulation and experimental results are in good agreement.**

***Index Terms*—Switched reluctance motor, nonlinear modeling, support vector regression, torque modeling, maximum correntropy criterion (MCC).**

I. Introduction

DUE to the increasing environmental pollution, electric vehicles (EVs) and hybrid electric vehicle (HEVs) are attractive substitutes to the traditional internal combustion engine vehicles [1,2]. In the motor drive systems, one of the main requirements is torque control [3,4]. Among numeral drive motors, permanent magnet synchronous motor [5-11] and switched reluctance motor (SRM) [12-14] are mainstream choices. The SRM shows its advantage and huge potential in the auto industry due to its simple and robust structure, low cost, high fault tolerance, high torque density and high efficiency in a wide range of speed [15-17]. However, its inherent double salient structure contributes to high nonlinearities both in its magnetic and torque characteristics [18,19]. Therefore, it is very difficult to derive its comprehensive mathematical model [20-22], and then it is harmful to provide the torque required by the vehicle accurately and quickly. Thereby, nonlinear modeling is demanded for accurate and fast calculation.

Researches on nonlinear modeling of SRM have mainly be concentrated in four techniques: 1) Experimental measurement techniques in which the value of inductance was measured directly [23]. This method has high accuracy since the data are measured under a dynamic environment, but the exclusive measuring equipment and tedious measuring process make it inconvenient. 2) Analytical modeling in which the numerical methods and finite element analysis (FEA) are not required, and it only requires the design parameters and the material properties [24]. Furthermore, the analytical modeling based on magnetic equivalent circuit [25], [26], and geometrical analysis [27] was also studied. 3) Finite element method, which has been used widely thanks to its accuracy. However, its computation time may be very long [28]. 4) Intelligent method.

The intelligent method is a popular approach in the field of nonlinear modeling owing to the emergence of numerous advanced intelligent algorithms. In [29,30], an adaptive neural fuzzy inference system and radial basis function network-based adaptive fuzzy system (RBFN-AFS) were utilized for modeling a 6/4 SRM respectively. The data were obtained from measurement. However, the fuzzy neural network usually acquires a local solution. In order to overcome this drawback, support vector machine (SVM) was used to obtain the entire flux linkage characteristics by training with the measured few samples in [31]. However, the computation time is long due to its quadratic programming. In [32], sparse least squares support vector machines (LSSVMs) were utilized to achieve nonlinear modeling for a precise motion of a planar SRM. Besides that, numerous researches were conducted to optimize the hyperparameters of LSSVM to improve the accuracy of the regression model, such as genetic algorithm (GA), particle swarm optimization (PSO), artificial bee colony (ABC)

This work was supported by the National Natural Science Foundation of China under Projects 51875261 and 51875255, the National Key Research and Development Program of China under Project 2017YFB0102603, the Natural Science Foundation of Jiangsu Province of China under Projects BK20180046, BK20170071, and BK20180100, the "Qinglan project" of Jiangsu Province, the Key Project of Natural Science Foundation of Jiangsu Higher Education Institutions under Project 17KJA460005, the Six Categories Talent Peak of Jiangsu Province under Projects 2015-XNYQC-003, and 2018-TD-GDZB-022, and Key Project for the Development of Strategic Emerging Industries of Jiangsu Province under Project 2016-1094. *(Corresponding author: Y. Cai and X. Chen.)*

X. Sun, J. Wu, Y. Cai and X. Chen are with the Automotive Engineering Research Institute, Jiangsu University, Zhenjiang 212013, China (email: xdsun@ujs.edu.cn, jlwu_ujs@163.com, caicaixiao0304@126.com, xbchen82@gmail.com).

G. Lei and Y. Guo are with the School of Electrical and Data Engineering, University of Technology Sydney, NSW 2007, Australia (e-mail: Gang.Lei@uts.edu.au, Youguang.Guo-1@uts.edu.au).

algorithm and differential evolution algorithm (DEA) [33–36]. Although those LSSVM algorithms were accurate and efficient, a potential drawback is that the solution may severely deviate from inlier samples if outliers exist, where inlier samples are the samples which are near the most normal samples and outliers are the samples which are markedly far away from the rest of sample. To reduce the interference of outliers, an adaptive weighted version of LSSVR is needed. The outliers which have large errors will be assigned smaller weights to reduce their interference. A recursive robust least squares support vector regression was proposed in [37]. Its hyperparameters are optimized by PSO. Its regression performance has been validated and compared with other intelligent algorithms. However, indeed, PSO has been proved to be poor in handling discrete optimization problems, and it is easy to acquire local optimum [38]. To solve this drawback, grey wolf optimization (GWO) algorithm, a new member of meta-heuristic algorithms proposed by Mirjalili in 2014 [39], can be used to optimize the hyperparameters. The philosophy of this optimization algorithm is inspired by the social behavior of grey wolves when they attack a prey. This algorithm moves the wolf group toward prey by updating the location vector, which is an average of the best locations of the group. It presents several advantages in terms of low computing complexity, high solution accuracy, convergence independence of initial conditions and ability to deal with local minima.

In this paper, the torque modeling of an SSRM using MCC-LSSVR is proposed. The comparisons are made with other intelligent methods. Then, simulation and experiment are conducted to validate the accuracy of the proposed model. The main contributions of this paper can be summarized in the following.

1) To reduce the interference of outlier, an adaptive weight LSSVR called MCC-LSSVR is utilized for the nonlinear model.

2) GWO is utilized to optimize the hyperparameters of MCC-LSSVR and then improve the computation efficiency.

3) Establish accurate and fast calculated flux linkage and torque models based on MCC-LSSVR and apply them into the steady-state operation, transient startup mode and varied load mode for effectiveness validation.

The remainder of this paper is organized as follows. Characteristics and mathematic model of SSRM are presented in Section II. Section III introduces the MCC-LSSVR. In Section IV, the MCC-LSSVR will be adapted for SSRM modeling. Simulation and experimental validations are presented in Section V, followed by conclusions.

II. Characteristics and Mathematical Model of SSRM

A. Mathematic topology of SSRM

Fig. 1 shows the machine topology of the proposed four-phase SSRM with 16/10 stator/rotor poles. As shown, the SSRM has 16 stator poles which include 8 excited poles and 8 auxiliary poles. The width of the excited pole is twice that of the auxiliary pole. The excited poles are wound by windings, while the auxiliary poles are only functioned as magnetic circuit without any windings. The rotor consists of ten separated segmented rotors which are evenly embedded in the nonmagnetic isolator. The basic operating principle and structural parameter optimization of the SSRM have been introduced in work [40]. The key parameters and dimensions of the SSRM are listed in Table I.

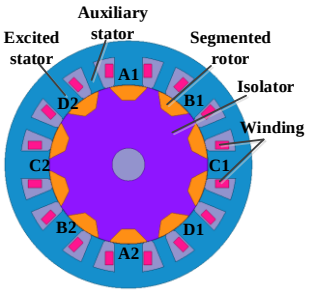

Fig. 1. Machine topology of the 16/10 SSRM.

TABLE I
KEY PARAMETERS AND DIMENSIONS OF THE SSRM

Parameters	Value	Parameters	Value
Number of phases	4	Stator yoke width (mm)	8
Rated speed (r/min)	6000	Rotor yoke width (mm)	5.5
Rated power (KW)	1.8	Stator pole arc (°)	21.375 /10.69
Stator outer diameter (mm)	128	Rotor pole arc (°)	26.64
Rotor outer diameter(mm)	82	Air gap length (mm)	0.25
Axial length (mm)	80	Number of turns in each pole	26

B. Mathematic model of SSRM

To reveal the nonlinear characteristics of the SSRM, the mathematic model of SSRM is introduced. First, the voltage equation of each phase is given by

$$U_m = Ri_m + \frac{d\psi_m}{dt} \tag{1}$$

where U_m, R, i_m, and Ψ_m are the phase m winding voltage, resistance, current and flux linkage respectively, t is the time. The general expression for the electromagnetic torque produced by one phase at any given current i_0 is

$$T_m(\theta, i_0) = \frac{\partial W_m'(\theta, i_0)}{\partial \theta}\Big|_{i_0 = const} \tag{2}$$

where W'_m and T_m, are the phase m winding co-energy and electromagnetic torque respectively, θ is rotor position angle.

The co-energy $W_m'(\theta, i_0)$ at any rotor position θ_0 is obtained from the saturation curves by

$$W_m'(\theta_0, i_0) = \int_0^{i_0} \psi_m(\theta_0, i) di \Big|_{\theta_0 = const} \tag{3}$$

According to the law of mechanics, the mechanical movement equation of the proposed SSRM can be obtained under the combined action of electromagnetic torque and load torque, which can be described as.

$$\sum_{m=1}^{n} T_m(\theta, i_m) = T_L + c_f \omega + J\frac{d\omega}{dt} \tag{4}$$

where J is the moment of inertia, ω mechanical angular velocity, θ rotor position angle, i_m phase m winding current, T_m the phase m electromagnetic torque, T_L the load torque, c_f

damping coefficient, and n the number of machine phases.

According to the above analysis, it is found that the relationship between total electromagnetic torque, phase current i_m and position angle θ is nonlinear. It is difficult to calculate the electromagnetic torque according to a given current and position angle.

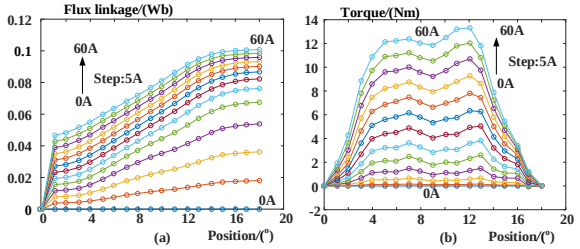

Fig. 2. FEA results of flux linkage and torque: (a) Flux linkage, and (b) Torque.

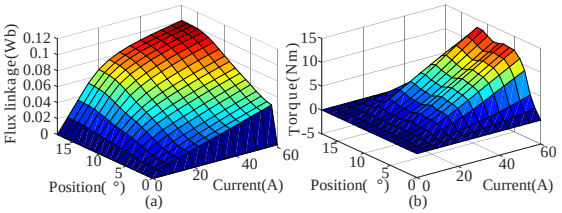

Fig. 3. Flux linkage and torque surfaces of SSRM: (a) Flux linkage, and (b) Torque.

C. FEA of SSRM

According to the above descriptions, the magnetic characteristics of SSRM can be appropriately modeled by equations defining the nonlinear flux linkage-current-angle (Ψ-i-θ) and torque-current-angle (T-i-θ) characteristics. In this section, FEA method of obtaining the flux linkage and torque is used to obtain the saturation curves of SSRM.

FEA is a numerical computational technique to determine the magnetic vector potential over complex geometric structures with magnetic nonlinearity. The analysis model is shown in Fig. 1. The main static characteristics of flux linkage and torque are given in Fig. 2. In order to visualize the nonlinear characteristics of flux linkage-current-angle (Ψ-i-θ) and torque-current-angle (T-i-θ), the surfaces are obtained and shown in Fig. 3.

III. Introduction of MCC-LSSVR

The flux linkage and torque of the SSRM are determined by the phase current i and rotor position θ and they are highly nonlinear functions. The LSSVR is an efficient method in the realm of soft computing. To tackle the problem of large noise and outliers, a novel regression model termed as MCC-LSSVR is proposed to acquire robust estimation for data in the presence of outliers. The regression model is combined with MCC, regularization technique and kernel trick in a unified framework. An iterative algorithm derived from half-quadratic optimization is further developed to solve the MCC-LSSVR with theoretically guaranteed convergence. Furthermore, a hyperparameters selection method for MCC-LSSVR is presented based on grey wolf optimization (GWO), such that multiple hyperparameters in MCC-LSSVR can be estimated effectively for better performance. The MCC-LSSVR is a very powerful algorithm in building a complex and nonlinear relationship between a set of input and output data. In this work, the flux linkage and torque data from FEA method are trained by the MCC-LSSVR.

A. Basis of LSSVR

Assume the given set of training samples $(x_i,y_i) \mid i=1,2,\ldots,m$, where n-dimensional input variable $x_i \in R^n$, and the output variable $y_i \in \mathrm{R}$.

First, the optimal regression model is set as

$$f(x) = w^T \cdot \phi(x) + b \tag{7}$$

where ϕ is a function which maps the input space to a higher dimensional feature space, w and b are the weight vector and bias term, respectively.

Then, the standardized cost function of LSSVM is

$$\begin{cases} \min\limits_{w,b,\xi} J(w,\xi) = \dfrac{1}{2}\|w\|^2 + \dfrac{C}{2}\sum\limits_{i=1}^{m}\xi_i^2 \\ s.t. \quad y_i = \omega^T\phi(x_i) + b + \xi_i, \quad i = 1,2,...,m \end{cases} \tag{8}$$

where C is a regularization parameter which balances the empirical risk and model complexity, and ξ_i is a fitting error.

In order to solve the problem, (8) is converted to the Lagrangian function:

$$L(w,b,\xi,\alpha) = J(w,\xi) - \sum_{i=1}^{n}\alpha_i\left(w^T\cdot\phi(x_i) + b + \xi_i - y_i\right) \tag{9}$$

where α_i is Lagrangian multiplier and (9) can be derived to (10) according to KKT (Karush-Kuhn-Tuchker) condition.

$$\begin{cases} \dfrac{\partial L}{\partial w} = 0 \rightarrow w = \sum\limits_{i=1}^{n}\alpha_i\cdot\phi(x_i) \\ \dfrac{\partial L}{\partial b} = 0 \rightarrow \sum\limits_{i=0}^{n}\alpha_i = 0 \\ \dfrac{\partial L}{\partial \xi_i} = 0 \rightarrow \alpha_i = C\xi_i \\ \dfrac{\partial L}{\partial \alpha_i} = 0 \rightarrow w^T\cdot\phi(x_i) + b + \xi_i - y_i = 0 \end{cases} \tag{10}$$

At last, w and ξ will be further eliminated by variable substitution and the following equation can be achieved.

$$\begin{bmatrix} K + C^{-1}I & e \\ e^T & 0 \end{bmatrix}\begin{bmatrix} \alpha \\ b \end{bmatrix} = \begin{bmatrix} Y \\ 0 \end{bmatrix} \tag{11}$$

where K is a kernel matrix with $K_{ij}=\phi(x_i)^T\ \phi(x_j) = K(x_i,x_j)$, $Y=[y_1, y_2, \ldots, y_m]^{\mathrm{T}}$, $e=[1,1,\ldots,1]^T$ and I is an identity matrix. By solving the unknown parameters α and b, another regression function of LSSVR model is obtained as follows

$$f(x) = \sum_{i=1}^{m}\alpha_i K(x,x_i) + b \tag{12}$$

Inputting the unknown vector x into the function (12), the corresponding output value $f(x)$ is obtained. The selection of kernel function $K(x_i,x_j)$ is a significant factor in LSSVR as it changes the model performance. In this paper, Gaussian kernel function (13) is selected to construct nonlinear LSSVR due to its excellent learning properties in a wide application.

$$K(x_i, x_j) = e^{-\|x_i - x_j\|^2 / \gamma^2} \tag{13}$$

where γ is the kernel or bandwidth parameter.

In order to obtain a robust estimation from data with outliers, it is essential to introduce an adaptive weight for each sample and this will be introduced in the following.

B. Maximum-correntropy-criterion-based LSSVR

Different from the conventional cost function which adopts sum of squares error (SSE) cost function, this paper develops a recursive robust LSSVR which is a combination of MCC and regularization in kernel space.

The correntropy is a generalized similarity measure between two arbitrary random variables, A and B. When the joint distribution of A and B is unknown and only a finite number of samples (a_i, b_i) i=1,2,…,m are given, the sample estimator of correntropy can be calculated as follows.

$$\hat{V}_\eta(A,B) = \frac{1}{m}\sum_{i=1}^{m} g(a_i - b_i, \sigma) \tag{14}$$

where

$$g(a-b,\sigma) = e^{-\frac{\|a-b\|^2}{\sigma^2}} \tag{15}$$

and (15) is the Gaussian kernel with bandwidth σ. It is worthy to note that (15) is utilized to measure the similarity between the predicted value and true target value while (13) represents a similarity between input variables.

Thus, the maximum of correntropy of error in (14) is called the MCC and it is a localized similarity measure compared with SSE which is a global one since the value of correntropy is mainly determined by the kernel function along the line, A=B.

Integrating MCC, regularization technique and kernel trick in a unified framework, (8) based on SSE can be transformed to

$$\max_{w,b} J(w,b) = \frac{C}{2}\sum_{i=1}^{m} g\left(w^T\cdot\phi(x_i)+b-y_i,\sigma\right) - \frac{1}{2}\|w\|^2 \tag{16}$$

To simplify (14) and the problem, which is brought by w with its high or even infinite dimensional feature space, a convex function φ is found which makes

$$g(x,\sigma) = \max_{p<0}\left(p\frac{\|x\|^2}{\sigma^2} - \varphi(p)\right) \tag{17}$$

and the maximum is obtained at p=-g(x, σ) when x is fixed.

Then the optimization problem (16) can be reconstructed with augmented objective function in enlarged parameter space as follows.

$$\max_{w,b,p} \bar{J}(w,b,p) = \frac{C}{2}\sum_{i=1}^{m}\left(p_i\frac{(w^T\cdot\phi(x_i)+b-y_i)^2}{\sigma^2} - \varphi(p_i)\right) - \frac{1}{2}\|w\|^2 \tag{18}$$

where p=[p_1, p_2,…, p_m]^T stores the auxiliary variables introduced in the half-quadratic optimization.

Combined with the restrictions as in the standard LSSVR, (18) can be converted to

$$\begin{cases} \max\limits_{w,b,\xi,p} \dfrac{C}{2}\sum\limits_{i=1}^{m}\left(p_i\dfrac{\xi^2}{\sigma^2} - \varphi(p_i)\right) - \dfrac{1}{2}\|w\|^2 \\ s.t. \quad y_i = \omega^T\phi(x_i) + b + \xi_i, \quad i = 1,2,...,m \end{cases} \tag{19}$$

At present, (19) can be iteratively optimized by alternatingly optimizing with respect to [w,b,ξ] and p while holding the other fixed.

First, hold p fixed and maximize (19) with respect to [w,b,ξ]. By eliminating the other unrelated variables and introducing variable q_i=-p_i, the equivalent problem can be obtained as follows.

$$\begin{cases} \min\limits_{w,b,\xi} \dfrac{C'}{2}\sum\limits_{i=1}^{m} q_i\dfrac{\xi_i^2}{\sigma^2} + \dfrac{1}{2}\|w\|^2 \\ s.t. \quad y_i = \omega^T\phi(x_i) + b + \xi_i, \quad i = 1,2,...,m \end{cases} \tag{20}$$

Compared with (8), the regularization parameter C has converted into $C'p_i/\sigma^2$. Imitate the solution of conventional LSSRV like (9)-(11), (21) can be obtained.

$$\begin{bmatrix} K+QI & e \\ e^T & 0 \end{bmatrix}\begin{bmatrix} \alpha \\ b \end{bmatrix} = \begin{bmatrix} Y \\ 0 \end{bmatrix} \tag{21}$$

The difference is that Q is a diagonal matrix whose diagonal Q_{ii}=(σ^2/$C'q_i$)=-(σ^2/$C'p_i$)>0 since p_i<0. K+QI is invertible as it is symmetric and positive-definite, (21) can be solved efficiently by the following equation

$$\begin{cases} b = \dfrac{e^T(K+Q)^{-1}Y}{e^T(K+Q)^{-1}e} \\ \alpha = (K+Q)\text{-}1(Y - eb) \end{cases} \tag{22}$$

Second, hold [w,b,ξ] fixed and optimize (18) with respect to p. Actually, according to (17), the optimal p is directly given by

$$p_i = -g(\xi_i,\sigma) = -\exp(-\frac{\xi_i^2}{\sigma^2}) \tag{23}$$

Considering that α_i=Cξ_i in (11) and C→ $C'p_i/\sigma^2$, the calculation formula of ξ_i is obtained as follows

$$\xi_i = -\frac{\sigma^2\alpha_i}{C'q_i} \tag{24}$$

So far, two sub-problems constituting the original optimization problem (19) have been solved. In order to describe the proposed MCC-LSSVR clearly, a schematic diagram is developed and shown in Fig. 4.

In Fig. 4, the initialization includes setting the parameter values p_i=q_i=-1 for all samples, tolerance ε=1×10^{-3}, correntropy parameter σ, kernel parameter γ, regularization parameter C', and building kernel matrix K.

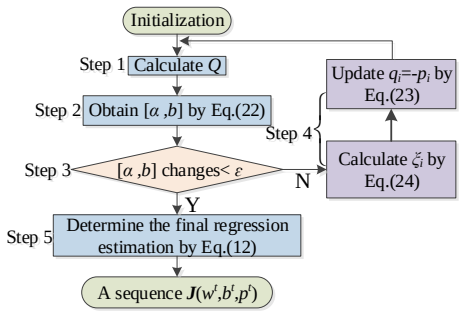

Fig. 4. Schematic diagram of MCC-LSSVR.

After introducing the schematic diagram of MCC-LSSVR and obtaining a sequence $\boldsymbol{J}(w^t,b^t,p^t)$, t=1,2,…The MCC-LSSVR is verified to be guaranteed to converge to its local optimal solution and its proof is followed.

According to steps 1 and 2, it can be obtained that $\boldsymbol{J}(w^t,b^t,p^t)\leq\boldsymbol{J}(w^{t+1},b^{t+1},p^t)$. Then, after performing step 3, $\boldsymbol{J}(w^{t+1},b^{t+1},p^t)\leq\boldsymbol{J}(w^{t+1},b^{t+1},p^{t+1})$. Hence, it can conclude that the sequence $\boldsymbol{J}(w^t,b^t,p^t)$, t=1,2,. . . is non-decreasing. Based on the property of correntropy, it can be verified that the objective function $\boldsymbol{J}(w,b,p)$ is bounded above since $g(a\text{-}b, \sigma)$ and $-\|w\|^2$ are both bounded above. Due to the above two facts and the well-known monotone convergence theorem, the algorithm is guaranteed to converge to its local optimal solution.

In conclusion, comparing (20) and (8), the former introduces an adaptive iterative weight in the latter because the error variable ξ_i^2 is weighted by a factor q_i. Besides that, according to (23), it is found that the weight will be smaller in the next iteration if the sample has a larger error, so its influence will be reduced. That is to say, the MCC-LSSVR is essentially an adaptive iterative weighted LSSVR.

C. GWO for hyper-parameter optimization of MCC-LSSVR

As shown from the above section, there are three hyperparameters including kernel parameter γ for the input space, kernel parameter σ for the output space and regularization parameter C' in MCC-LSSVR, and they need to be optimized. Besides that, several times are needed to obtain the final solution of MCC-LSSVR by solving (21). Thus, the computation of MCC-LSSVR on every hyper-parameter combination is time-consuming, which restricts the application of the conventional grid-based model selection technique. In order to resolve the model selection problem, a GWO based hyper-parameter selection algorithm for MCC-LSSVR is proposed in this section.

The GWO process includes the social hierarchy stratification, tracking, enveloping and attacking prey of grey wolf (GW). The steps are as follows.

Step 1: Social Hierarchy. Build a grey wolf social hierarchy model. Calculate the fitness of each individual in the population, and mark the three GWs with the best fitness in the wolves as *E*, *F*, *G*, and the remaining GWs are marked as *H*.

Step 2: Encircling Prey. GW gradually approaches the prey and surrounds it when it searches for prey. The mathematical model of this behavior is as follows.

$$\begin{cases} D = C_r * X_p(\tau) - X(\tau) \\ X(\tau+1) + X_p(\tau) - A * D \\ A = 2a * r_1 - a \\ C_r = 2r_2 \end{cases} \tag{25}$$

where τ is the iteration, * is Hadamard product, A and C_r are the coefficients of synergy, X_p is the position vector of the prey, $X(\tau)$ is the position vector of the current GW, a is linearly reduced from 2 to 0 throughout the iteration, and r_1 and r_2 are random vectors between 0 to 1

Step 3: Hunting. During each iteration, keep the three best GWs (*E*, *F*, *G*) in the current population and then update the location of other search agents including *H* based on their location information. The mathematical model of this behavior can be expressed as follows.

$$\begin{cases} D_E = C_{r1} * X_E - X, D_F = C_{r2} * X_F - X, \\ D_G = C_{r3} * X_G - X, \ X_1 = X_E - A_1 * D_E, \\ X_2 = X_F - A_2 * D_F, \ X_3 = X_G - A_3 * D_G \\ X(\tau+1) = (X_1 + X_2 + X_3)/3 \end{cases} \tag{26}$$

where X_E, X_F, X_G represent the position vectors of *E*, *F*, *G* in the current population respectively; X represents the GW position vector; D_E, D_F, D_G respectively indicate the distance between the current candidate GW and the three best wolves, When $|A|$ >1, the GWs are scattered among the regions and search for prey. When |A|<1, the grey wolf will focus on hunting for prey in one or some areas.

Step 4: Attacking Prey. When constructing the attack prey model, according to (26), the decrease of a causes the value of A to fluctuate accordingly. If A is in the interval [-1,1], the next moment of the search agent can be anywhere between the current GW and the prey.

Step 5: Search for Prey. GWs rely mainly on information about *E*, *F*, *G* to find prey. They began to search for prey location information and then are concentrated to attack prey. For the establishment of the decentralized model, the search agent is kept away from the prey by $|A|$>1. This search method enables GWO to perform global search. Another search coefficient in the GWO algorithm is C_r. From (26), the C_r vector is a vector of random values over the interval range [0, 2], which provides a random weight for the prey to increase or decrease. This benefits GWO to demonstrate random search behavior during the optimization process to avoid the algorithm being partially optimal.

According to the above introduction of GWO, an algorithm to handle the hyperparameters selection problem for MCC-LSSVR is proposed and the specific optimization process is described in Fig. 5.

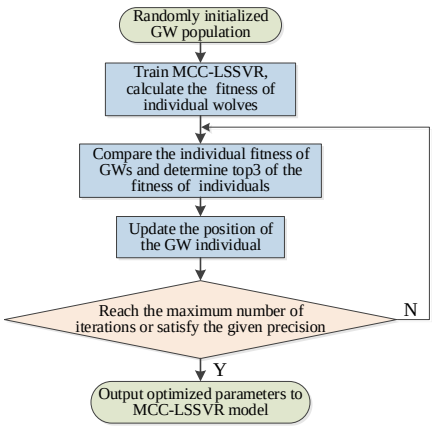

Fig. 5. Specific optimization process of MCC-LSSVR based on GWO.

The parameters of the GWO algorithm implemented in Fig.5 have been set to achieve a good tradeoff between convergence and the use of allocated resources (agents, iterations). The total number of agents is 20, the maximum number of iterations is 100, and it randomly generates a population of particles composed of γ, σ and C' in [0.1, 10].

IV.4. Application of MCC-LSSVR for SSRM Modeling

A. Algorithm verification

Since the main drawback of the SRM is the high torque ripple

To verify the effectiveness and superiority of the proposed MCC-LSSVR, especially in the existence of outliers, the comparisons are made with other algorithms, such as RBFN-AFS in [24], SVM in [25] and LSSVR in [26]. The evaluation indexes such as mean absolute error (MAE) and root mean square error (RMSE) are utilized to evaluate the accuracy of the proposed model. Their definitions are

$$\mathrm{MAE} = \max_{j=1}^{n} \left| y_j - y_{j0} \right| \tag{27}$$

$$\mathrm{RMSE} = \sqrt{\frac{1}{n}\sum_{j=1}^{n}(y_j - y_{j0})^2} \tag{28}$$

where y_j is the regression of the output and y_{j0} is the sample data.

Although both the MAE and RMSE can measure the error between the predicted and true target values, the MAE is less sensitive to large forecast errors. Therefore, when the testing samples are affected by outliers, the MAE should be preferred as a performance evaluation criterion.

In the algorithm verification, the training samples are generated by the following Sinc function which is widely used in regression analysis.

$$f(x) = \mathrm{sinc}(x) = \begin{cases} \dfrac{\sin \pi x}{\pi x} & x \neq 0 \\ 1 & x = 0 \end{cases} \quad x \in [-5, 5] \tag{29}$$

To effectively validate the anti-interference performance of the MCC-LSSVR, noises are added to the training samples as outliers. Specifically, the training samples combined with outliers are generated as follows.

$$y_i = \mathrm{sinc}(xi) + \zeta, \zeta \sim D_\delta = (1-\delta)G + \delta H,\ 0 \le \delta \le 1 \tag{30}$$

where gross error model D_δ is a linear combination of normal noise distribution G and outliers symmetric long-tailed distribution H, δ is used to adjust the percentage of outliers in the training samples, and ζ is noise. In the validation, b0th G and H follow Gaussian distribution $N(a, b^2)$ with mean a and standard deviation (STD) b. As for the normal noise, G is fixed as $N(0, 0.1^2)$, whereas for the outliers, H is set as $N(0, b^2)$ with $b>>0$. By doing so, different kinds of polluted datasets can be generated by adjusting the parameter b and outlier percentage δ.

Assume b=1, H follows $N(0,1^2)$ and change the value of δ approximately from 10% to 40% with a 10% step and investigate the performance of those methods under the sets of different outlier percentages. Fig. 6(a) shows one-run fitting results of RBFN-AFS, SVM, LSSVR and the proposed MCC-LSSVR when outlier ratio δ=10%. Obviously, MCC-LSSVR derives better approximation compared with the other methods. Fig. 6(b) shows the results when the outlier percentage δ=30%. Table II lists the average results over 10 independent runs of four methods on datasets with different outlier percentages. It can be found that the proposed MCC-LSSVR shows the best performance consistently on all the datasets. Actually, even under high outlier proportion, MCC-LSSVR still has remarkably small RMSE compared with its competitors.

As introduced above, MCC-LSSVR is an adaptive weighting method by nature and the final weight factor q_i for each sample are shown in Fig. 7. It can be noted that different samples have different weights on the basis of their outlying degree. The more outlying is a sample, the smaller weight it has. Therefore, the influence of these outliers is reduced and the final regressor trends to approximate those normal samples. It is why the MCC-LSSVR can maintain high accuracy with the existence of outliers.

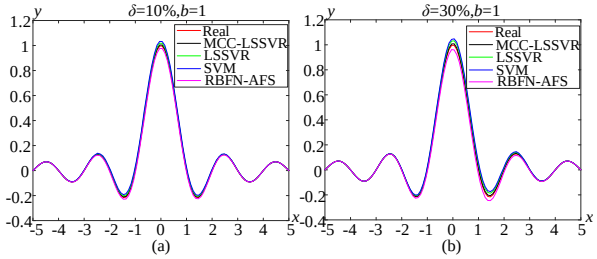

Fig. 6. Fitting results of RBFN-AFS, SVM, LSSVR and the proposed MCC-LSSVR when outlier ratio (a) δ=10%, and (b) δ=30%.

TABLE II
COMPARISON RESULTS OF DIFFERENT ALGORITHMS WITH DIFFERENT OUTLIER PERCENTAGE

Outlier	RBFN-AFS [24]		SVM [25]	
ratio	MAE	RMSE	MAE	RMSE
10%	0.0836	0.0987	0.0912	0.1032
20%	0.1169	0.1487	0.1354	0.1512
30%	0.1328	0.1635	0.1523	0.1702
40%	0.1664	0.1895	0.1936	0.2103
Outlier	LSSVR [26]		MCC-LSSVR	
ratio	MAE	RMSE	MAE	RMSE
10%	0.0709	0.0955	0.0325	0.0250

20%	0.1069	0.1357	0.0523	0.0352
30%	0.1135	0.1457	0.0756	0.0441
40%	0.1370	0.1702	0.0853	0.0481

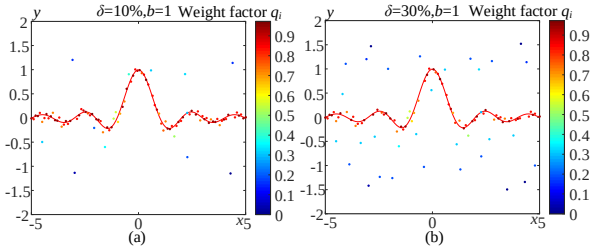

Fig. 7. Weight factor q_i in MCC-LSSVR on simulated dataset when (a) δ=10%, and (b) δ=30%.

B. Specific implementation

To train the MCC-LSSVR model, the date $[\theta, i, \Psi]$ and $[\theta, i, T]$ are obtained by FEA as shown in Fig. 3, and the hyper-parameters are optimized by using the GWO. Then, acquire the regression parameters α_i, b which make the MCC-LSSVR model with the fitting results. After the training, input any i and θ, the corresponding Ψ or T will be obtained. Taking torque T as an example, the schematic diagram is shown in Fig. 8.

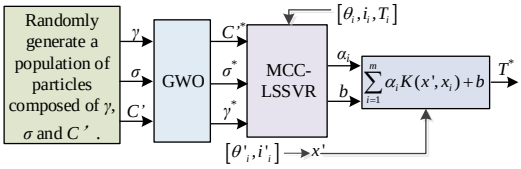

Fig. 8. MCC-LSSVR model based on GWO utilized for torque regression.

Via the regression of MCC-LSSVR model, the phase flux linkage and torque surfaces versus the rotor position θ and phase current i are shown in Fig. 9. Besides, the computational time t_c of phase flux linkage and torque are recorded to reflect the computational load burden on the processors.

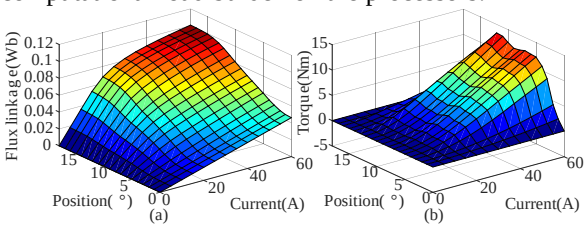

Fig. 9. Flux linkage and torque surfaces based on MCC-LSSVR model: (a) flux linkage, and (b) torque.

C. Model verification and evaluation

To verify the accuracy of the MCC-LSSVR model of SSRM, the evaluation indexes MAE and RMSE are utilized to evaluate the accuracy of the proposed model. Besides, according to the conclusions deduced by Section 4.1, the nature of the sample data used in the model can have a large outlier proportion, and the difference between the outlier value and the normal value should not exceed 40% to ensure adequate model accuracy.

In this paper, the estimation of the output flux linkage Ψ_j and torque T_j, and the sample data flux linkage Ψ_{j0} and torque T_{j0}, are obtained with the same phase current i and position angle θ, and then the errors $\Delta\Psi$ and ΔT are calculated as shown in Fig. 10.

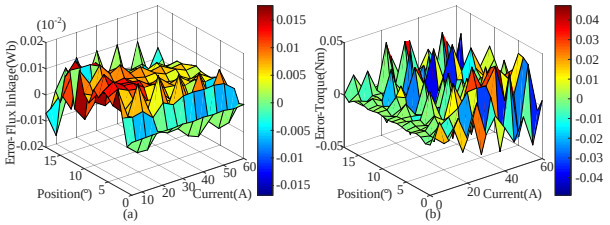

Fig. 10. The error between estimation of the output and sample data: (a) Flux linkage, and (b) Torque.

TABLE III
COMPARISON RESULTS OF DIFFERENT INTELLIGENT MODELING

Modeling methods	Flux linkage/10^{-2}Wb			Torque/Nm		
	MAE	RMSE	Time(s)	MAE	RMSE	Time(s)
RBFN-AFS [24]	0.0962	0.0862	5.8	0.1134	0.1089	7.3
SVM [25]	0.0846	0.0756	9.6	0.1008	0.0925	12.5
LSSVR [26]	0.0424	0.0306	8.5	0.0525	0.0494	11.4
MCC-LSSVR	0.0086	0.0073	2.4	0.0252	0.0189	3.6

As shown in Fig. 10, the MAEs of flux linkage and torque are 0.0176×10^{-2} Wb and 0.042 Nm, respectively, the RMSEs are 0.0073×10^{-2} Wb and 0.0189 Nm, respectively, and the computational times are 2.4 s and 3.6 s respectively.

To verify the superiority of the MCC-LSSVR model, comparisons are made by simulation with other models. The evaluation indexes are the MAE, RMSE and computational times. The comparison results are listed in Table III. As shown, the MCC-LSSVR model of SSRM appears more effective than the others. This confirms the results of algorithm verification in Section 4.1.

V. Simulation and Experimental Validation

In order to verify the accuracy of the proposed model in terms of steady-state operation, transient startup operation and varied load operation, the chopped current control (CCC) mode at low speed, the angle position control (APC) mode at high speed, startup mode and varied load mode will be adopted. The comparison will be made in terms of simulation and experiment in this section. The main difference is the methods for the calculation of flux linkage and torque. One uses the data obtained by FEA to make a look-up table, then calculate flux linkage and torque directly by interpolation. Another uses the proposed nonlinear model to obtain flux linkage and torque directly.

A. Simulation results validation

Fig. 11 shows the simulation block diagram which includes a current reference block, four phase models of SSRM and mechanical motion equation from a holistic perspective. From a certain phase perspective, it contains four other blocks which are the Switch, Look-up $i(\psi,\theta)$, Look-up $T(i,\theta)$ and Modulo $\pi/5$, respectively.

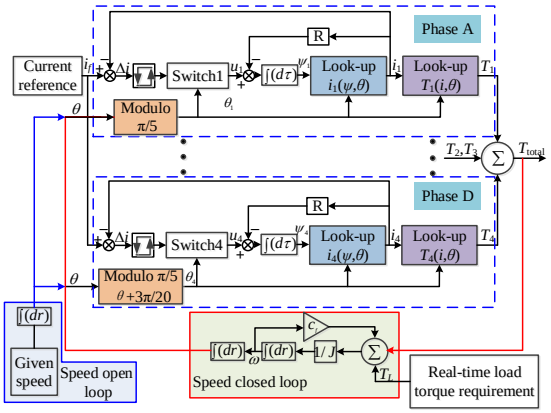

Fig. 11. Simulation block diagram of dynamic performance validation.

Switch block controls the power converter commutation via receiving the current demand signal Δi and position signal θ. Look-up $i(\psi,\theta)$ modules estimate the current from flux linkage ψ and rotor position θ for each phase. In Section IV (part A), the flux linkage surface based on MCC-LSSVR model has been obtained and is shown in Fig. 9 (a). In order to facilitate the construction of the model, the MCC-LSSVR $\psi(i,\theta)$ model is transformed to $i(\psi,\theta)$ via inverting the relationship between i and ψ by angle θ one by one, and the training result is shown in Fig. 12.

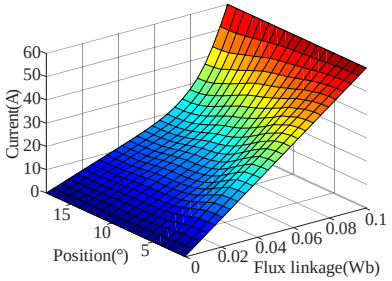

Fig. 12. Current surface based on MCC-LSSVR model.

Look-up $T(i,\theta)$ modules output the regression torque via the input of current signal i and position signal θ.

Modulo π/5 block is utilized to compensate for the position angle difference between phases. π/5 is the periodicity of the phase flux linkage and torque, and π/20 is the phase difference.

1) Steady-State operation validation

Under the CCC mode, the DC voltage is 120 V, the reference current is 75 A, the hysteresis current bandwidth is 5 A, the given rotor speed is 600 rpm, and the turn on and turn off angles are 20° and 35° respectively. The speed loop is an open loop and can be adjusted manually. The comparison results are shown in Fig. 13, where different colors represent different phases. As shown, at low speed, the current, flux linkage and total torque waveforms are chopped obviously, and the results run by the MCC-LSSVR model agree well with the results run by measured data. Besides, the total torque is large, which benefits the start-up of the motor.

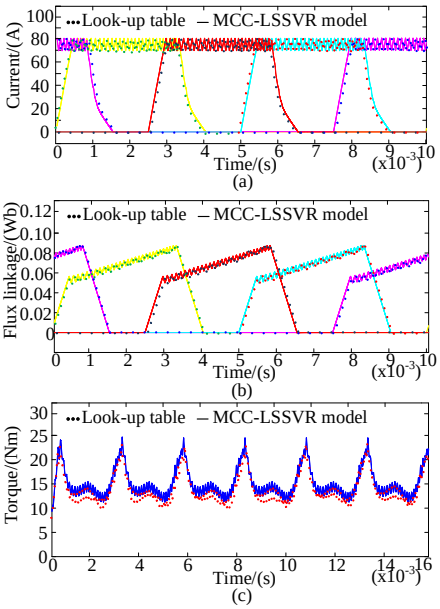

Fig. 13. Performance comparison under CCC mode: (a) Current, (b) Flux linkage, and (c) Total torque.

Under the APC mode, the given rotor speed is set as the rated speed of 6000 rpm, and other initial parameters are the same as those in CCC mode. The compared results are shown in Fig. 14, where the different colors represent different phases. As shown, at high speed, the current, flux linkage and total torque waveforms are all in good agreement. Besides, compared with the waveforms of CCC mode, they decline obviously.

2) Transient startup mode validation

For the dynamic transient startup operation validation, the difference from the steady-state operation validation is that the speed loop is closed loop. The load is set as 1 Nm and other initial parameters are the same as those in CCC mode. The comparison results are shown in Fig. 15. As shown, the speed and current curves of the two models are in good agreement, and the MCC-LSSVR exhibits fast startup performance.

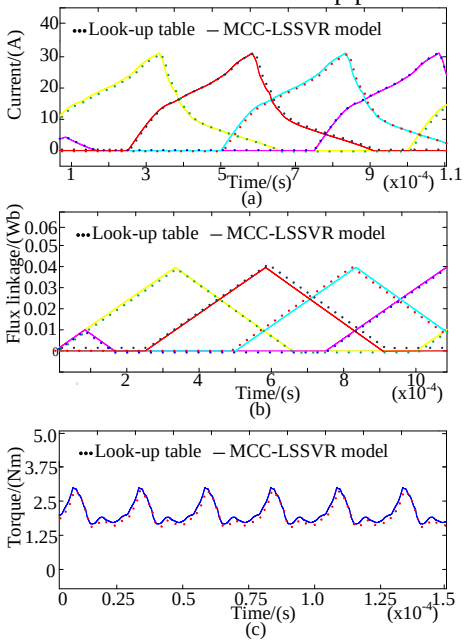

Fig. 14. Performance comparison under APC mode: (a) Current, (b) Flux linkage, and (c) Total torque.

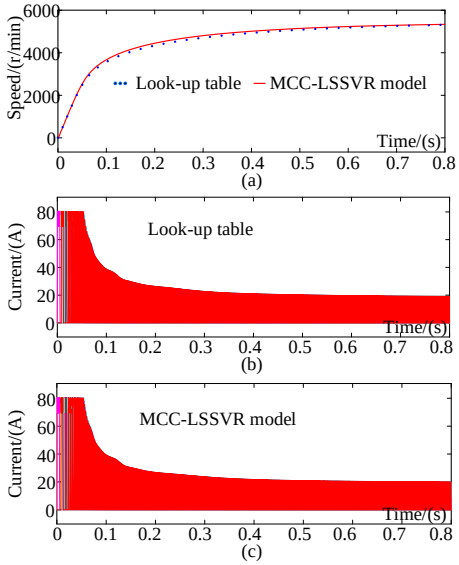

Fig. 15. Performance comparison under transient Startup Operation: (a) Speed, (b) Current of measured model, and (c) Current of MCC-LSSVR model.

3) Varied load mode validation

In order to simulate the practical varying load mode in the operation of EVs, the load torque requirements are set as 15 Nm at 1 s, 10 Nm at 3 s, 5 Nm at 5 s, and all loads keep 2 s. For other time, the torque is set as 0. From the simulated analysis, it is found that the torque provided by the motor of MCC-LSSVR model shows shorter response time and lower torque ripple than that of the measured model as shown in Fig. 16.

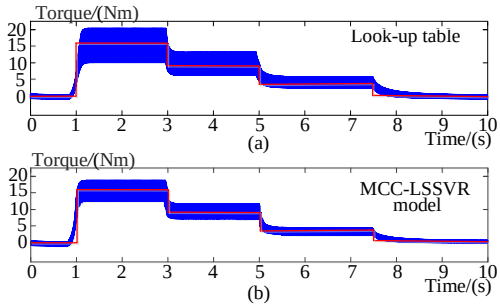

Fig. 16. Performance comparison under varying load mode: (a) Look-up model, and (b) MCC-LSSVR model.

B. *Experimental results validation*

After verifying the model through simulation, the experimental comparison follows to validate the accuracy of the MCC-LSSVR model in practical operations. Fig. 17 shows the test devices and platform for the dynamic characteristics, where the 16/10 poles SSRM prototype, JN338 torque and speed sensor with 20 Nm torque range, and FZ25J magnetic power brake with 25 Nm torque range are connected by two couplings. The position is detected by the Hall sensor ATS675LSE and then the signal is sent to the dSPACE. Similarly, the current signal captured by the current sensor is also sent to the dSPACE for further control. Other hardwares include a DC power supply, an asymmetrical half-bridge circuit, PC and oscilloscope. The detailed experimental setup is shown as a block diagram in Fig. 18. Since the control strategy in the dSPACE controller board is compiled from the Matlab/Simulink via code generation and download software, the specific experimental parameters are the same as the simulation parameters.

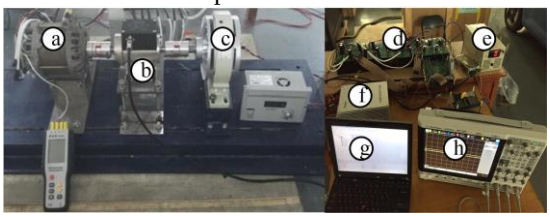

Fig. 17. Devices and platform for testing dynamic characteristics: (a) 16/10 SSRM, (b) Torque and speed sensor, (c) Magnetic power brake, (d) Power converter and drive circuit, (e) Power supply, (f) dSPACE, (g) PC, and (h) Oscilloscope.

During the experiment, the current and torque models which are in the simulation block diagram switch from measured model to MCC-LSSVR model. The CCC and APC modes switch according to the given rotor speed, and the startup mode is established individually. In order to make a fair and intuitive comparison between the measured model and MCC-LSSVR model, the sampling method and speed are the same. Meanwhile, vertically, the value indicated by each cell of the oscilloscope is the same. The experimental results under CCC mode at 600 rpm, APC mode at 6000 rpm, startup mode and varying load mode are shown in Figs. 19-22, respectively. As shown, the waveforms of current and total torque appear to have similar amplitude and frequency between measured and MCC-LSSVR model for both CCC mode and APC mode. Actually, if the waveforms are amplified it can be discovered that the waveforms obtained by MCC-LSSVR model are obviously smoother than those obtained by measured model, especially the total torque waveform. Besides, the results of transient startup mode and varying load mode also validate the effectiveness and superiority of the proposed MCC-LSSVR model.

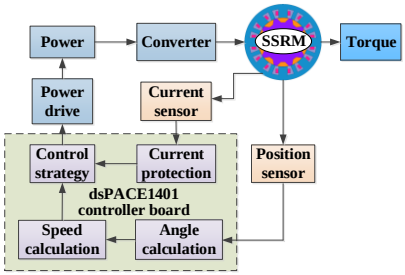

Fig. 18. Block diagram of the experimental setup.

During the experiment, the current and torque models which are in the simulation block diagram switch from measured model to MCC-LSSVR model. The CCC and APC modes switch according to the given rotor speed, and the startup mode is established individually. In order to make a fair and intuitive comparison between the measured model and MCC-LSSVR model, the sampling method and speed are the same. Meanwhile, vertically, the value indicated by each cell of the oscilloscope is the same. The experimental results under CCC mode at 600 rpm, APC mode at 6000 rpm, startup mode and varying load mode are shown in Figs. 19-22, respectively. As shown, the waveforms of current and total torque appear to have similar amplitude and frequency between measured and MCC-LSSVR model for both CCC mode and APC mode. Actually, if the waveforms are amplified it can be discovered that the waveforms obtained by MCC-LSSVR model are obviously

smoother than those obtained by measured model, especially the total torque waveform. Besides, the results of transient startup mode and varying load mode also validate the effectiveness and superiority of the proposed MCC-LSSVR model.

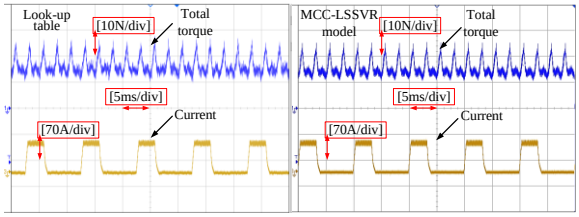

Fig. 19. Experimental results comparison under CCC mode at 600 rpm.

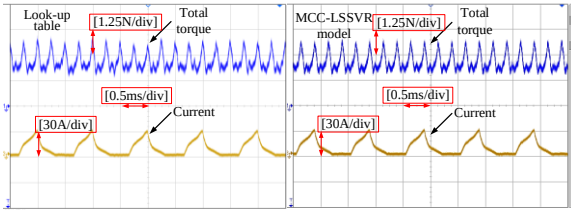

Fig. 20. Experimental results comparison under APC mode at 6000 rpm.

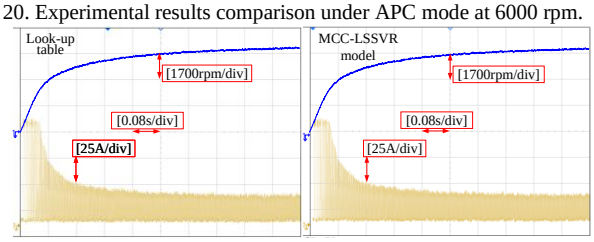

Fig.21. Experimental results comparison under transient startup mode.

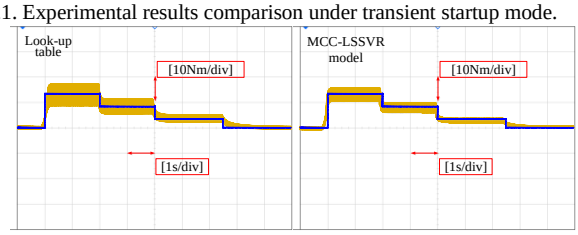

Fig. 22. Experimental results comparison under varying load mode.

VI. Conclusion

In this paper, to provide the torque required by the vehicle accurately and quickly, an advanced nonlinear model named MCC-LSSVR was employed to regress the nonlinear characteristics of the flux linkage and torque of a 16/10 SSRM. The specific main conclusions of this paper are shown as follows.

1) The proposed MCC-based LSSVR has an adaptive weight and can reduce the interference of outliers. Thereby, the established nonlinear models of phase flux linkage and torque of SSRM based on MCC-LSSVR algorithm show smaller calculation error and shorter calculation time than other algorithms.

2) The established nonlinear models based on MCC-LSSVR algorithm can be well applied in various operation modes, such as steady-state operation, transient startup mode, and varying load mode.

3) The application of the proposed torque modeling method is effective. Besides, the provided torque utilizing MCC-LSSVR model shows shorter response time and lower torque ripple than that utilizing the measured model. This is consistent with the conclusion that the calculation error is smaller and the calculation time is shorter than other algorithms.

Thus, it can be concluded that the MCC-LSSVR model shows the nonlinear characteristics of SSRM well such as flux linkage and torque, which is conducive for accurate and fast calculation in actual control.

References

[1] X. Sun, Z. Shi, G. Lei, Y. Guo, and J. Zhu. "Analysis, design and optimization of a permanent magnet synchronous motor for a campus patrol electric vehicle," *IEEE Trans. Veh. Technol.*, vol. 68, no. 11, pp. 10535-10544, Nov. 2019.

[2] Z. Shi, *et. al*. "Analysis and optimization of radial force of permanent magnet synchronous Hub motors," *IEEE Trans. Magn.*, vol. 56, no. 2, Feb. 2020, Art. no.: 7508804.

[3] C. Liu, J. Zhu, Y. Wang and et al. "Cogging torque reduction of SMC PM machine using shifted and un-equal stator teeth", *IEEE trans. applied superconductivity*, vol. 117, no. 4, article#5204704, 2016.

[4] C. Liu, J. Lu, Y. Wang, G. Lei, J. Zhu and Y. Guo. "Techniques for Reduction of the Cogging Torque in Claw Pole Machines with SMC Cores", *Energies*, vol. 10, no. 10, article#1541, 2017.

[5] X. Sun, C. Hu, G. Lei, Y. Guo, and J. Zhu. "State feedback control for a PM hub motor based on grey wolf optimization algorithm," *IEEE Trans. Power Electron.*, vol. 35, no. 1, pp. 1136-1146, Jan. 2020.

[6] Q. Chen, W. Zhao, G. Liu and Z. Lin, "Extension of virtual-signal-injection-based MTPA control for five-phase IPMSM into fault-tolerant operation," *IEEE Trans. Ind. Electron.*, vol. 66, no. 2, pp. 944-955, Feb. 2019.doi: 10.1109/TIE.2018.2826473

[7] X. Zhu, J. Huang, L. Quan, Z. Xiang, and B. Shi. "Comprehensive sensitivity analysis and multi-objective optimization research of permanent magnet flux-intensifying motors," *IEEE Trans. Ind. Electron.*, vol. 66, no. 4, pp. 2613-2627, Apr. 2019.

[8] X. Sun, Z. Shi, G. Lei, Y. Guo, and J. Zhu, "Multi-objective design optimization of an IPMSM based on multilevel strategy," *IEEE Trans. Ind. Electron.*, 2020, DOI: 10.1109/TIE.2020.2965463.

[9] Q. Chen, G. Xu, F. Zhai and G. Liu, "A novel spoke-type PM motor with auxiliary salient poles for low torque pulsation," *IEEE Trans. Ind. Electro.*, DOI: 10.1109/TIE.2019.2924864.

[10] X. Sun, J. Cao, G. Lei, Y. Guo, and J. Zhu, "Speed sensorless control for permanent magnet synchronous motors based on finite position set," *IEEE Trans. Ind. Electron.*, 2020, DOI: 10.1109/TIE.2019.2947875.

[11] X. Zhu, M. Jiang, Z. Xiang, L. Quan, W. Hua, and M. Cheng, "Design and optimization of a flux-modulated permanent magnet motor based on an airgap-harmonic-orientated design methodology," *IEEE Trans. Ind. Electron.*, DOI: 10.1109/TIE.2019.2934063.

[12] X. Sun, K. Diao, Z. Yang, G. Lei, Y. Guo, and J. Zhu, "Direct torque control based on a fast modeling method for a segmented-rotor switched reluctance motor in HEV application," *IEEE J. Emerg. Sel. Topics Power Electron.*, 2020, DOI: 10.1109/JESTPE.2019.2950085.

[13] N. R. Patel, V. A. Shah, and M. M. Lokhande, "A novel approach to the design and development of 12/15 radial field C-core switched reluctance motor for implementation in electric vehicle application," *IEEE Trans. Veh. Technol.*, vol. 67, no. 9, pp. 8031-8040, Jan. 2018.

[14] X. Sun, K. Diao, and Z. Yang, "Performance improvement of a switched reluctance machine with segmental rotors for hybrid electric vehicles," *Comput. Electr. Eng.*, vol.77, pp. 244-259, Jul. 2019.

[15] K. Kiyota, T. Kakishima, A. Chiba, and M. A. Rahman, "Cylindrical rotor design for acoustic noise and windage loss reduction in switched reluctance motor for HEV applications," *IEEE Trans. Ind. Appl.*, vol. 52, no. 1, pp. 154-162, Jan. 2016.

[16] M. Asgar and E. Afjei, "Radial force reduction in a new flat-type double-stator switched reluctance motor," *IEEE Trans. Energy Convers.*, vol. 31, no. 1, pp. 141-149, Mar. 2016.

[17] K. Diao, X. Sun, G. Lei, Y. Guo, and J. Zhu, "Multiobjective system level optimization method for switched reluctance motor drive systems using finite element model," *IEEE Trans. Ind. Electron.*, 2020, DOI: 10.1109/TIE.2019.2962483.

[18] G. Cao, N. Chen, S. Huang, S. Xiao, and J. He, "Nonlinear modeling of the flux linkage in 2-D plane for the planar switched reluctance motor," *IEEE Trans. Mag.*, vol. 54, no. 11, pp. 1-5, Nov. 2018.

[19] J. B. Bartolo, M. Degano, J. Espina, and C. Gerada, "Design and initial testing of a high-speed 45-kW switched reluctance drive for aerospace

application," *IEEE Trans. Ind. Electron.*, vol. 64, no. 2, pp. 988-997, 2017.
[20] F. J. Perez-Cebolla, A. Martinez-Iturbe, B. Martín-del-Brío, C. Bernal, and A. Bono-Nuez, "Nonlinear lumped-circuit model for switched reluctance motors exhibiting core losses," *IEEE Trans. Ind. Electron.*, vol. 63, no. 6, pp. 3433-3445, 2016.
[21] X. Sun, K. Diao, G. Lei, Y. Guo, and J. Zhu, "Real-time HIL emulation for a segmented-rotor switched reluctance motor using a new magnetic equivalent circuit," *IEEE Trans. Power Electron.*, vol. 35, no. 4, pp. 3841-3849, Apr. 2020.
[22] R. Madhavan and B. G. Fernandes, "Axial flux segmented SRM with a higher number of rotor segments for electric vehicles," *IEEE Trans. Energy Convers.*, vol. 28, no. 1, pp. 203-213, Mar. 2013.
[23] P. Zhang, P. Cassani, and S. Williamson, "An accurate inductance profile measurement technique for switched reluctance machines," *IEEE Trans. Ind. Electron.*, vol 57, no. 9, pp. 2972-2979, Sep. 2010.
[24] W. Uddin and Y. Sozer, "Analytical modeling of mutually coupled switched reluctance machines under saturation based on design geometry," *IEEE Tran. Ind. Appl.*, vol 53, no. 5, pp. 4431-4440, Sep. 2017.
[25] X. Sun, Y. Shen, S. Wang, G. Lei, Z. Yang, and S. Han, "Core losses analysis of a novel 16/10 segmented rotor switched reluctance BSG motor for HEVs using nonlinear lumped parameter equivalent circuit model," *IEEE/ASME Trans. Mechatronics*, vol. 23, no. 2, pp. 747-757, Apr. 2018.
[26] F. Perez and A. Martinez, "Nonlinear lumped-circuit model for switched reluctance motors exhibiting core losses," *IEEE Trans. Ind. Electron.*, vol 63, no. 6, pp. 3433-3445, Jun. 2016.
[27] C. Xia, M. Xue, and T. Shi, "A new rapid nonlinear simulation method for switched reluctance motors," *IEEE Trans. Energy Convers.*, vol 24, no. 3, pp. 578-586, Sep. 2009.
[28] J. Dong, B. Howey, B. Danen, J. Lin, J. W. Jiang, B. Bilgin, and A. Emadi, "Advanced dynamic modeling of three-phase mutually coupled switched reluctance machine," *IEEE Trans. Energy Convers.*, vol. 33, no. 1, pp. 146-154, Mar. 2018.
[29] W. Ding and D. Liang, "Modeling of a 6/4 switched reluctance motor using adaptive neural fuzzy inference system," *IEEE Trans. Mag.*, vol. 44, no. 7, pp. 1796-1804, Jan. 2008.
[30] D. Liang and W. Ding, "Modelling and predicting of a switched reluctance motor drive using radial basis function network-based adaptive fuzzy system," *IET Elec. Power Appl.*, vol. 3, no. 3, pp. 218-230, May 2009.
[31] S. Song, L. Ge, and M. Zhang, "Data-reconstruction-based modeling of SRM with few flux-linkage samples from torque-balanced measurement," *IEEE Trans. Energy Convers.*, vol. 31, no. 2, pp. 424-435, Jun. 2016.
[32] S. Huang, G. Cao, Z. He, J. F. Pan, J. Duan, and Q. Qian, "Nonlinear modeling of the inverse force function for the planar switched reluctance motor using sparse least squares support vector machines," *IEEE Trans. Ind. Inform.*, vol. 11, no. 3, pp. 591-600, Jun. 2015.
[33] W. Shang, S. Zhao, Y. Shen, "Application of LSSVM with AGA optimizing parameters to nonlinear modeling of SRM," *Proceedings of the Third IEEE Conference on Industrial Electronics and Applications*, pp. 775–780, 2008.
[34] Q. Xiang, Y. Sun, X. Ji, "Modeling Inductance for Bearingless Switched Reluctance Motor based on PSO-LSSVM," *Proceedings of the Chinese Control and Decision Conference (CCDC)*, pp. 800–803, 2011.
[35] S.J. Evangeline, S.S. Kumar, J. Jayakumar, "Nonlinear modeling of a switched reluctance motor using LSSVM–ABC," *J. Appl. Sci. Acta Polytech. Hung.* vol. 11, no. 6, pp. 143–158, Jun. 2015.

[36] S. Jebarani, S. Suresh, and J. Jayakumar, "Torque modeling of switched reluctance motor using LSSVM-DE," *Neurocomputing*, vol. 211, no. 26, pp. 117-128, Feb. 2016.
[37] X. Chen, J. Yang, and J. Liang, "Recursive robust least squares support vector regression based on maximum correntropy criterion," *Neurocomputing*, vol. 97, no. 15, pp. 63-73, Nov. 2012.
[38] S. U. Khan, S. Yang, L. Wang, and L. Liu, "A modified particle swarm optimization algorithm for global optimizations of inverse problems," *IEEE Trans. Magn.*, vol. 52, no. 3, pp. 1-4, 2016.
[39] S. Mirjalili, S. Mohammad, and A. Lewis, "Grey wolf optimizer," *Adv. Eng. Software*, vol. 69, pp. 46–61, 2014.
[40] X. Sun, K. Diao, G. Lei, L. Chen, Y. Guo, and J. Zhu, "Study on segmented-rotor switched reluctance motors with different rotor pole numbers for BSG system of hybrid electric vehicles," *IEEE Trans. Veh. Technol.*, vol. 68, no. 6, pp. 5537-5547, Jun. 2019.

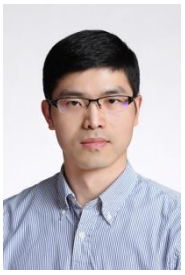

Xiaodong Sun (M'12-SM'18) received the B.Sc. degree in electrical engineering, and the M.Sc. and Ph.D. degrees in control engineering from Jiangsu University, Zhenjiang, China, in 2004, 2008, and 2011, respectively.

Since 2004, he has been with Jiangsu University, where he is currently a Professor with the Automotive Engineering Research Institute. From 2014 to 2015, he was a Visiting Professor with the School of Electrical, Mechanical, and Mechatronic Systems, University of Technology Sydney, Sydney, Australia. His current teaching and research interests include electrical machines and drives, drives and control for electric vehicles, and intelligent control. He is the author or coauthor of more than 80 refereed technical papers and one book, and he is the holder of 36 patents in his areas of interest.

Jiangling Wu received the B.Eng. degree in Vehicle engineering from Jiangsu University, Zhenjiang, China, in 2018, and is currently working toward the M. Eng. degree at Jiangsu University, Zhenjiang, China.

His current research interests include modeling, structure designing and controlling of switched reluctance motors for electric vehicle propulsion.

Gang Lei (M'14) received the B.S. degree in Mathematics from Huanggang Normal University, China, in 2003, the M.S. degree in Mathematics and Ph.D. degree in Electrical Engineering from Huazhong University of Science and Technology, China, in 2006 and 2009, respectively. He is currently a senior lecturer at the School of Electrical and Data Engineering, University of Technology Sydney (UTS), Australia. His research interests include design optimization and control of electrical drive systems and renewable energy systems.

Yingfeng Cai (M'17) received the B.S., M.S. and Ph.D. degree all from the School of Instrument Science and Engineering, Southeast University, Nanjing, China, respectively. In 2013, she joined the Automotive Engineering Research Institute in Jiangsu University, now she is a professor. Her research interests include computer vision, intelligent transportation systems and intelligent automobiles.

Xiaobo Chen received the Ph.D. degree in pattern recognition and intelligent systems from Nanjing University of Science & Technology (NJUST), China, in 2013. From March to August 201 l, he served as a research assistant at the Hong Kong Polytechnic University (PolyU), Hong Kong. From April 2015 to August 2017, he served as a postdoctoral research associate at the University of North Carolina at Chapel Hill (UNC-CH), USA. He is currently an associate professor at automotive engineering research institute, Jiangsu University, China. His major research interests concentrate on sensor fusion, target tracking and machine learning. He has published more than 70 papers in numerous international journals and conference proceedings.

Youguang Guo (S'02-M'05-SM'06) received the B.E. degree from Huazhong University of Science and Technology, China in 1985, the M.E. degree from Zhejiang University, China in 1988, and the Ph.D. degree from University of Technology, Sydney (UTS), Australia in 2004, all in electrical engineering. He is currently a professor at the School of Electrical and Data Engineering, University of Technology Sydney (UTS). His research fields include measurement and modeling of properties of magnetic materials, numerical analysis of electromagnetic field, electrical machine design optimization, power electronic drives and control.